



# Electrochemical performance of graphene oxide modified graphite felt as a positive electrode in all-iron redox flow batteries

M. S. Anantha<sup>1,2</sup> · D. Anarghya<sup>1,2</sup> · Chunyan Hu<sup>3,4</sup> · Narendra Reddy<sup>1</sup> · Krishna Venkatesh<sup>1</sup> · H. B. Muralidhara<sup>1</sup>

Received: 14 March 2020 / Accepted: 17 September 2020 / Published online: 28 September 2020  
© Springer Nature B.V. 2020

## Abstract

In this study, we demonstrate that coating a layer of graphene oxide (GO) onto graphite felts (GF) by electrostatic spraying can substantially increase the performance of all-iron redox flow batteries (IRFBs). Graphite felts are extensively used as electrodes but they do not have the desired electrochemical properties. GO has good electrochemical features. Hence, GO was synthesized from graphite powder and applied onto graphite felts. Chemical and structural features of the bare graphite felt electrode (BGF), thermally treated graphite felt electrode (TTGF), and graphene oxide modified graphite felt electrode (GOMGF) were characterized using X-Ray Diffraction (XRD), Scanning Electron Microscopy (SEM), Energy Dispersive X-Ray Analysis (EDX), Transmission Electron Microscopy (TEM), Raman Spectroscopy (RS), X-Ray Photoelectron Spectroscopy (XPS) and Brunauer–Emmett–Teller (BET) surface area analysis. Similarly, the electrochemical performance was evaluated using Cyclic Voltammetry (CV), Electrochemical Impedance Spectroscopy (EIS), Tafel analysis and charge–discharge experiments. The Charge–discharge experiments were performed at 1 to 5 mgcm<sup>-2</sup> weight of GO on the modified graphite felt electrode and varying the current densities from 10 to 40 mAcm<sup>-2</sup>. The coulombic efficiency ( $\eta_C$ ) and energy efficiency ( $\eta_E$ ) of the cell determined at 20 mAcm<sup>-2</sup> for 4 mgcm<sup>-2</sup>-GOMGF electrodes were found to be 64.61% and 50.27%, respectively. Among the three different types of electrodes, the GOMGF electrode showed better electrocatalytic performance mainly due to the excellent conducting network of the defective edges of oxygen on the surface of layered flakes of the GO. After twenty cycles, the average  $\eta_C$  and  $\eta_E$  of the cell using a 4 mgcm<sup>-2</sup>-GOMGF electrode were found to be 62.06% and 42.02%, respectively.

---

✉ H. B. Muralidhara  
hb.murali@gmail.com

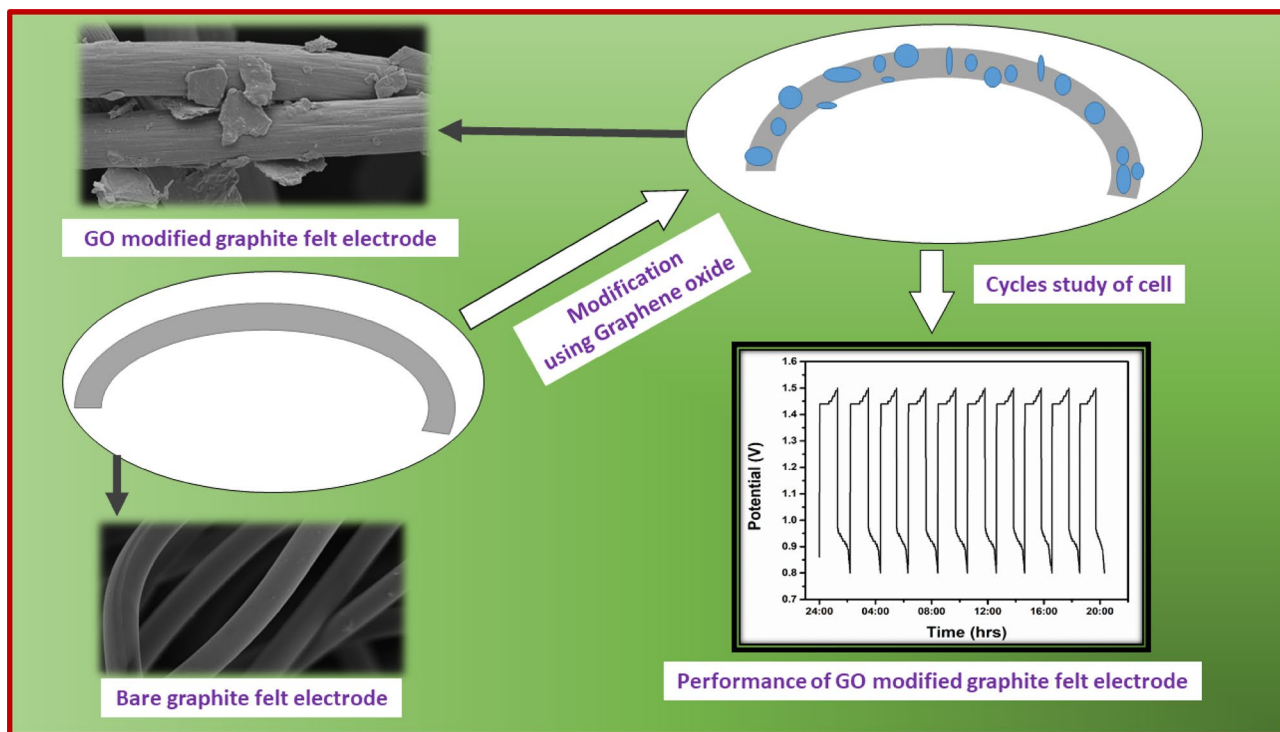
<sup>1</sup> Centre for Incubation, Innovation, Research and Consultancy (CIIRC), Jyothy Institute of Technology, Thataguni, Off Kanakapura Road, Bangalore, Karnataka 560082, India

<sup>2</sup> Research Resource Centre, Jnana Sangama, Visvesvaraya Technological University, Belagavi, Karnataka 590018, India

<sup>3</sup> College of Chemistry, Chemical Engineering and Biotechnology, Donghua University, Shanghai 201620, People's Republic of China

<sup>4</sup> National Engineering Research Center for Dyeing and Finishing of Textiles, Donghua University, Shanghai 201620, People's Republic of China

## Graphic abstract

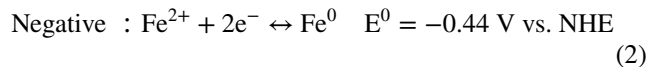
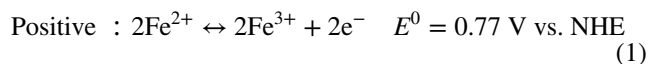


**Keywords** Graphene oxide · Electrocatalyst · Graphite felt · Coulombic efficiency

## 1 Introduction

Renewable energy sources such as wind and solar are intermittent and unpredictable [1, 2] in terms of their output, which is dependent on several environmental factors. Also, it becomes difficult to expand or distribute all the energy when it is produced in excess or more than expected. Hence, storing energy when there is excess availability becomes a necessity. Several energy storage systems (ESS) have been developed to harvest and store energy, similar to storing energy for domestic purposes [3]. However, most of these storage systems have limited capacity, are expensive or use non-renewable, environmentally unfriendly materials and processes. Redox flow batteries are one of the common energy storage systems which have several advantages [4–8]. Unlike conventional batteries, redox flow batteries have a unique design, construction, storage capacity and flexibility [9]. In a redox flow battery, the electrolytes are stored in reservoirs and redox reactions occur as the liquid electrolyte flows through the cell. As the quantity of the electrolyte increases, the capacity to store energy increases [10]. Potentially, the capacity of a redox flow battery can be increased up to the megawatt-hour level, which makes it very attractive for large scale and grid-level storage applications [11].

Among different types of RFB systems, IRFBs are considered to be more efficient and preferable for grid-level storage. In IRFBs,  $\text{Fe}^{2+}/\text{Fe}^{3+}$  and  $\text{Fe}^{2+}/\text{Fe}$  act as positive and negative electrolytes, respectively. A typical reaction occurring in the IRFBs is given in Eqs. 1–3. As seen from the equations,



The use of ligand supported electrolytes will help in the prevention of precipitation of the electrolyte as ferrous hydroxide. Previously, reports have described that ascorbic acid, an organic acid containing two electrons, reduces the oxidation of  $\text{Fe}^{3+}/\text{Fe}^{2+}$  [12]. It is also mentioned in the literature that both ascorbic acid and its oxidized forms, hinder the hydrogen evolution, and enhances the performance of the battery [13].

Electrodes are the critical components in any RFB systems [14], since the composition, structure and performance of the electrode are crucial for achieving high-efficiency batteries. Considerable attention has been paid to develop

appropriate electrodes or modify the electrodes using metal oxides [15], rare earth oxides [16], carbon catalysts [17], functionalized organic materials [18], heteroatom-doped catalysts [19], etc. These materials act as electrocatalysts in the modified electrodes and increase the effective redox reactions by exchanging ions and charges.

Graphene oxide is extensively used to modify electrodes and improve the performance of redox flow batteries. For instance, thermally reduced GO and different structures containing GO shows enhancement in the performance of the cell and increases the stability of the graphite felt electrodes toward the redox flow batteries [20–22]. The availability of large surface area and effective reactive sites or edges are the main reasons for the enhanced electrochemical and catalytic activity of GO.

In this study, GO modified graphite felts were used as positive electrode in IRFBs. The GOMGF electrode showed significant enhancement of coulombic efficiency ( $\eta_c$ ) compared to bare graphite felt electrode (BGF), thermally treated graphite felt electrode (TTGF). To the best of our knowledge, there are no reports on electrode modification and performance characterization using iron electrolytes.

## 2 Experimental

### 2.1 Materials and methods

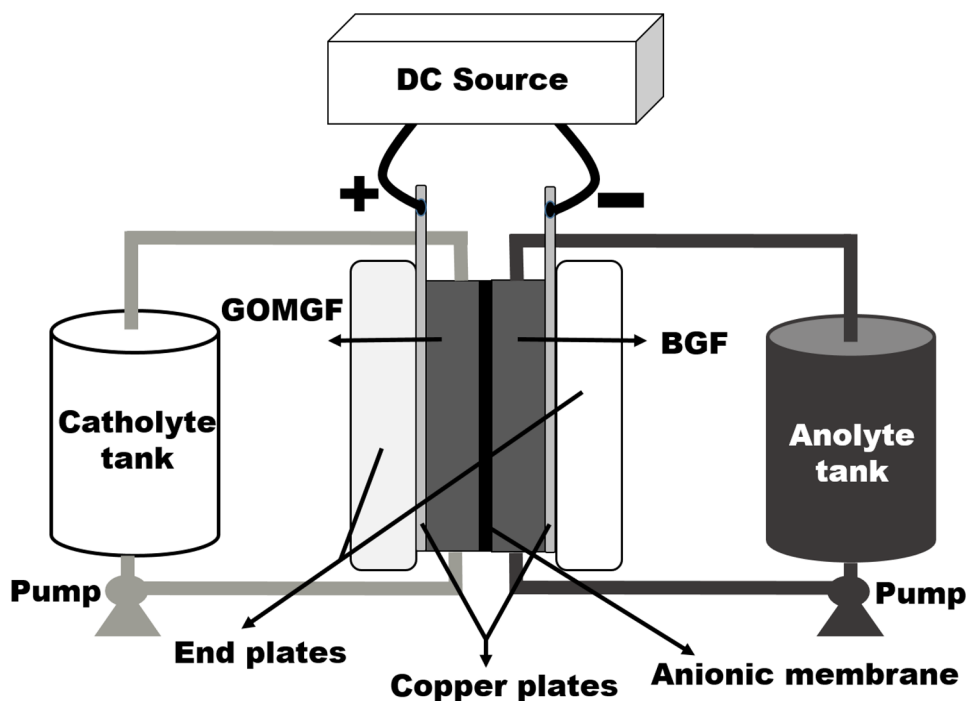
Graphite powder, sulfuric acid ( $H_2SO_4$ ), phosphoric acid ( $H_3PO_4$ ), potassium permanganate ( $KMnO_4$ ), hydrogen

peroxide ( $H_2O_2$ ), hydrochloric acid (HCl), ferrous chloride ( $FeCl_2$ ), ascorbic acid ( $C_6H_8O_6$ ), ammonium chloride ( $NH_4Cl$ ) and absolute alcohol ( $C_2H_5OH$ ) was purchased from Bangalore Scientific and Industrial Supplies, Bangalore, India. All chemicals were used as received, without further purifications. The graphite felt electrode was purchased from Rayon Graphite felt (AGFHT), USA. The anionic membrane (FUMASEP FAP- 375PP) and Nafion binder used were obtained from Fuel Cell Store, USA. The battery components such as reinforced epoxy endplates of 15 mm thickness, copper plates and gaskets were fabricated in-house, graphite serpentine flow fields were machined with the help of a local vendor M/s Mersen India Pvt. Ltd., Bangalore. A schematic of the battery components and assembled system is shown in Fig. 1.

### 2.2 Preparation of GO by modified Hummer's method

GO was synthesized from pure graphite powder using modified Hummer's method. A 30 ml mixture of  $H_2SO_4$  and  $H_3PO_4$ , was prepared in a 9:1 ratio and stirred for a specified time. Pure graphite powder (0.225 g) was added into the beaker containing the mixture of the two acids. Later, 1.32 g of  $KMnO_4$  was slowly added and the mixture was stirred continuously for 6 h. During this process, the color of the solution changes from brownish to dark green indicating the formation of GO.  $H_2O_2$  (0.7 ml) was added dropwise to remove the excess volume of  $KMnO_4$  in the solution. Later, the solution was allowed to cool and centrifuged to

**Fig. 1** A typical assembly of the IRFBs



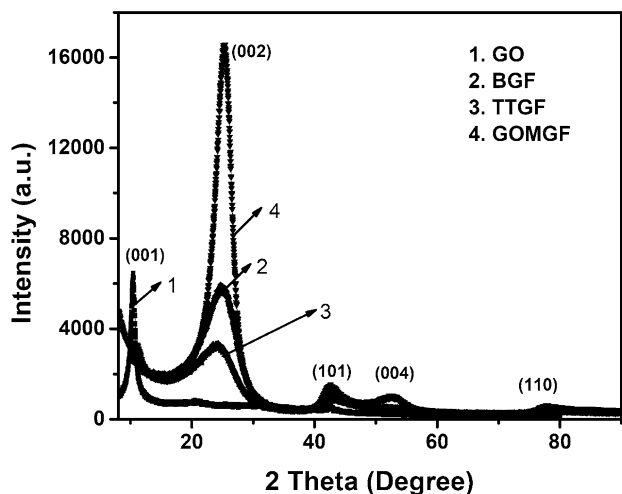


Fig. 2 XRD spectra of GO, BGF, TTGF and GOMGF electrodes

precipitate the GO. The residue obtained was washed with dilute HCl followed by deionized water. The washing process was repeated 3–4 times and the obtained GO was dried in an oven at 363 K for 24 h [23].

### 2.3 Modification of BGF

A known quantity of GO was dispersed in alcohol by continuous stirring at room temperature using a magnetic stirrer for about 5 h (350 rpm). Nafion (5wt %) was added to the above solution and sonicated for about 15 min. Later, either side of the BGF was coated with GO using 1.4 mm internal diameter nozzle spray gun (Aimex H-827) at an air pressure of 58 PSI. Coated electrodes were vacuum dried for about 24 h maintaining a temperature of 353 K and pressure 25 PSI.

### 2.4 Characterizations

XRD studies of the GO, unmodified and modified electrodes were carried out on an eco D8 Advance Bruker XRD system (Cu  $K_{\alpha}$  radiation source,  $\lambda = 0.154$  nm). The morphology of the GO, BGF, TTGF, GOMGF electrodes was analyzed using SEM (SEM-JEOL JSM 840A) and elemental analysis was performed using EDAX at 20 kV. Raman spectra of BGF, TTGF and GOMGF electrodes were analyzed using (HORIBAJOBINYVON LABRAM) with 532 nm LASER at an exposure time of 5 s. A charge-coupled device (CCD) was used as a detector for the analysis with 1800 lines/mm grating. XPS analysis was carried out using (KRATOS-AXIS ULTRA DLD) with Al- $K_{\alpha}$  radiation (1486.6 eV). The determination of specific surface area, pore volume and pore diameter were done on ASAP 2010 Micrometrics instrument.

## 2.5 Electrochemical studies

CV, EIS (frequency range: 0.01 to  $10^5$  Hz) and Tafel analysis were carried out using an electrochemical work station (CHI600E Series) with a conventional three-electrode system. The working electrodes used in the studies were BGF, TTGF, GOMGFs, Ag/AgCl electrode as a reference electrode and platinum is a counter electrode.  $FeCl_2$  solution was prepared using deionized water and used as the electrolyte. All the experiments were performed under ambient room temperature.

## 2.6 Charge–discharge studies

A single-cell having 132  $cm^2$  active area with GOMGF and BGF positive and negative electrodes, respectively, were used for the charge–discharge studies (Fig. 1). FUMASEP FAP-375PP was used as a separator.

The iron-electrolyte was prepared using a mixture of 3.25 M  $FeCl_2$ , 0.3 M  $C_6H_8O_6$  and 1.0 M  $NH_4Cl$  with deionized water. Here,  $C_6H_8O_6$  acts as ligand and reduces the pH imbalance of the electrolytes.  $NH_4Cl$  increases the conductivity of the  $FeCl_2$  electrolyte. The iron-electrolyte stored in glass reservoirs acts as anolyte and catholyte and was connected to the redox flow cell using a rubber hose. The flow of the electrolyte into the cell was controlled at 130  $ml\ min^{-1}$  using a peristaltic pump (RH-P100L-200-2H-1D). The charge–discharge and cycling studies were carried out using the Bitrode life cycle tester (LSV 1-100/0.1-47) by varying the current density from 10 to 40  $mA\ cm^{-2}$  and potential between 0.8 and 1.5 V. Coulombic ( $\eta_C$ ), voltaic ( $\eta_V$ ) and energy ( $\eta_E$ ) efficiencies were calculated using the following equations:

$$\text{Coulombic efficiency} = \frac{\text{Discharge current} \times \text{Discharge Time}}{\text{Charge current} \times \text{Charge Time}} \times 100 \quad (4)$$

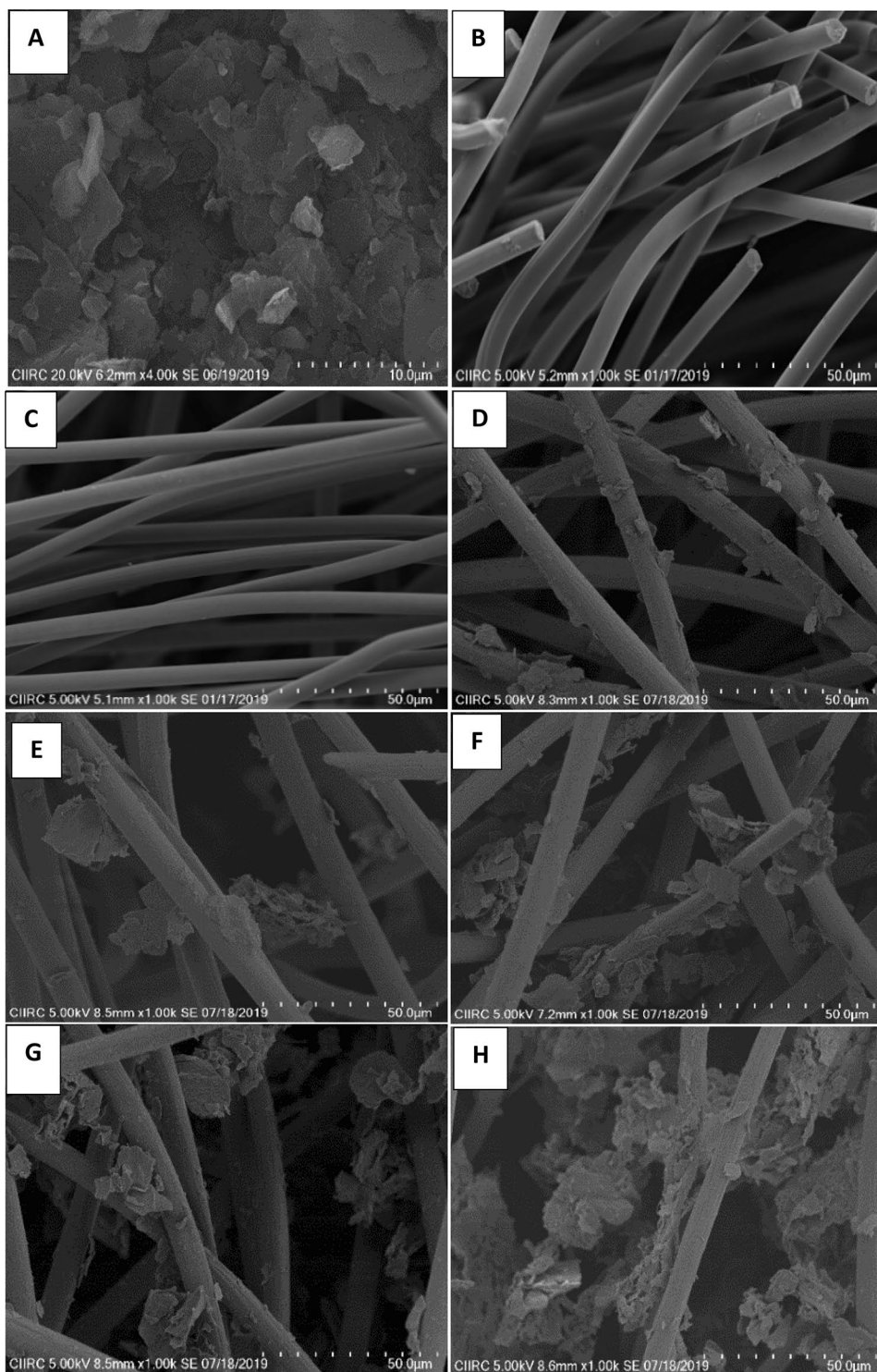
$$\text{Voltaic efficiency} = \frac{\text{Average discharge voltage}}{\text{Average charge voltage}} \times 100 \quad (5)$$

$$\text{Energy efficiency} = \frac{\text{Discharge current} \times \text{Discharge Time} \times \text{Discharge voltage}}{\text{Charge current} \times \text{Charge Time} \times \text{Charge voltage}} \times 100 \quad (6)$$

## 3 Results and discussion

The XRD spectra of GO, BGF, TTGF and 4  $mg\ cm^{-2}$ -GOMGF electrodes are shown in Fig. 2. GO showed an intense peak at  $10.0^\circ$  which is indexed to be (001) lattice plane and considered to be caused by the

**Fig. 3** SEM images of **a** GO, **b** BGF electrode, **c** TTGF electrode, **d** 1 mgcm<sup>-2</sup>-GOMGF electrode, **e** 2 mgcm<sup>-2</sup>-GOMGF electrode, **f** 3 mgcm<sup>-2</sup>-GOMGF electrode, **g** 4 mgcm<sup>-2</sup>-GOMGF electrode, **h** 5 mgcm<sup>-2</sup>-GOMGF electrode, and **i** EDAX spectrum of 4 mgcm<sup>-2</sup>-GOMGF electrode



presence of oxygen functional groups attached to either side of the graphene sheets [24]. This peak has good agreement with the pure graphene oxide JCPDS file number-00-065-1528. The crystalline phases of BGF, TTGF and 4 mgcm<sup>-2</sup>-GOMGF show diffraction peaks at 25.31°, 42.59°, 52.59°, and 77.98° representing the hkl planes (002), (101), (004), (110), respectively. The

intensity of peaks decreased in TTGF compared to BGF due to oxidation of the GF during the thermal treatment. However, the intensity of the peak at 10.0° and 25.31° increases in 4 mgcm<sup>-2</sup>-GOMGF due to the deposition of GO on the surface of GF (Pure graphite, JCPDS file number-00-04-1487). In 4 mgcm<sup>-2</sup>-GOMGF electrode, the presence of a small peak at 10.0° confirms the deposition

Fig. 3 (continued)

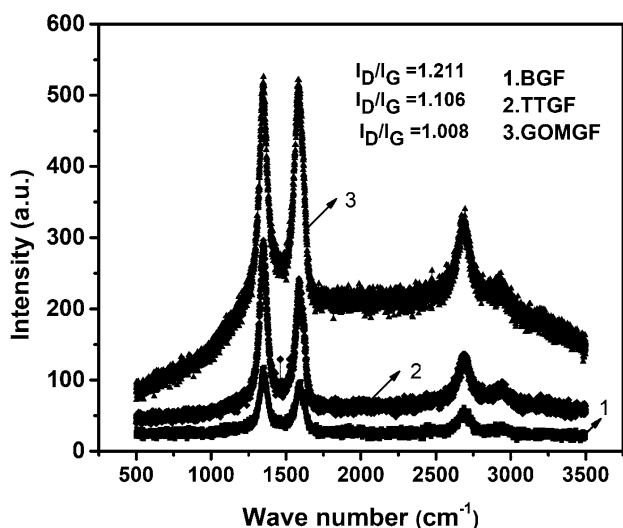
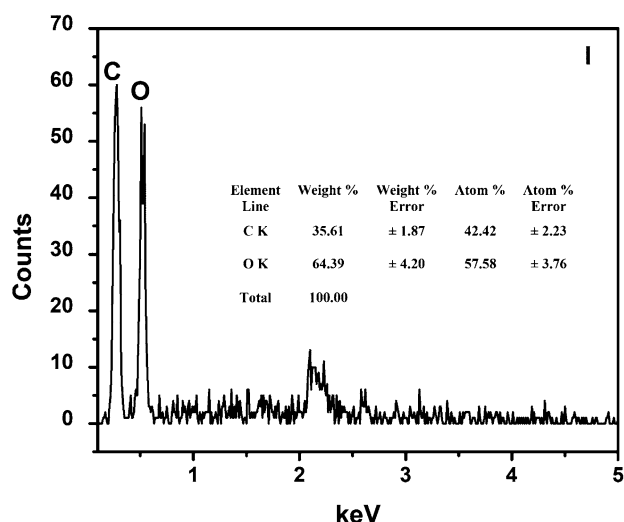


**Fig. 4** Raman spectra of BGF, TTGF and GOMGF electrodes (Excitation at 532 nm)

of GO on the surface of the GF with a hexagonal crystal structure. Using Scherrer's equation, the average crystal size of GO in the 4 mgcm<sup>-2</sup>-GOMGF electrode was determined for a high-intensity peak from the XRD spectra. The crystal size of GO in the 4 mgcm<sup>-2</sup>-GOMGF electrodes was found to be 6.76 nm. The nano GO increases the electrochemical and catalytic activity toward the redox reactions.

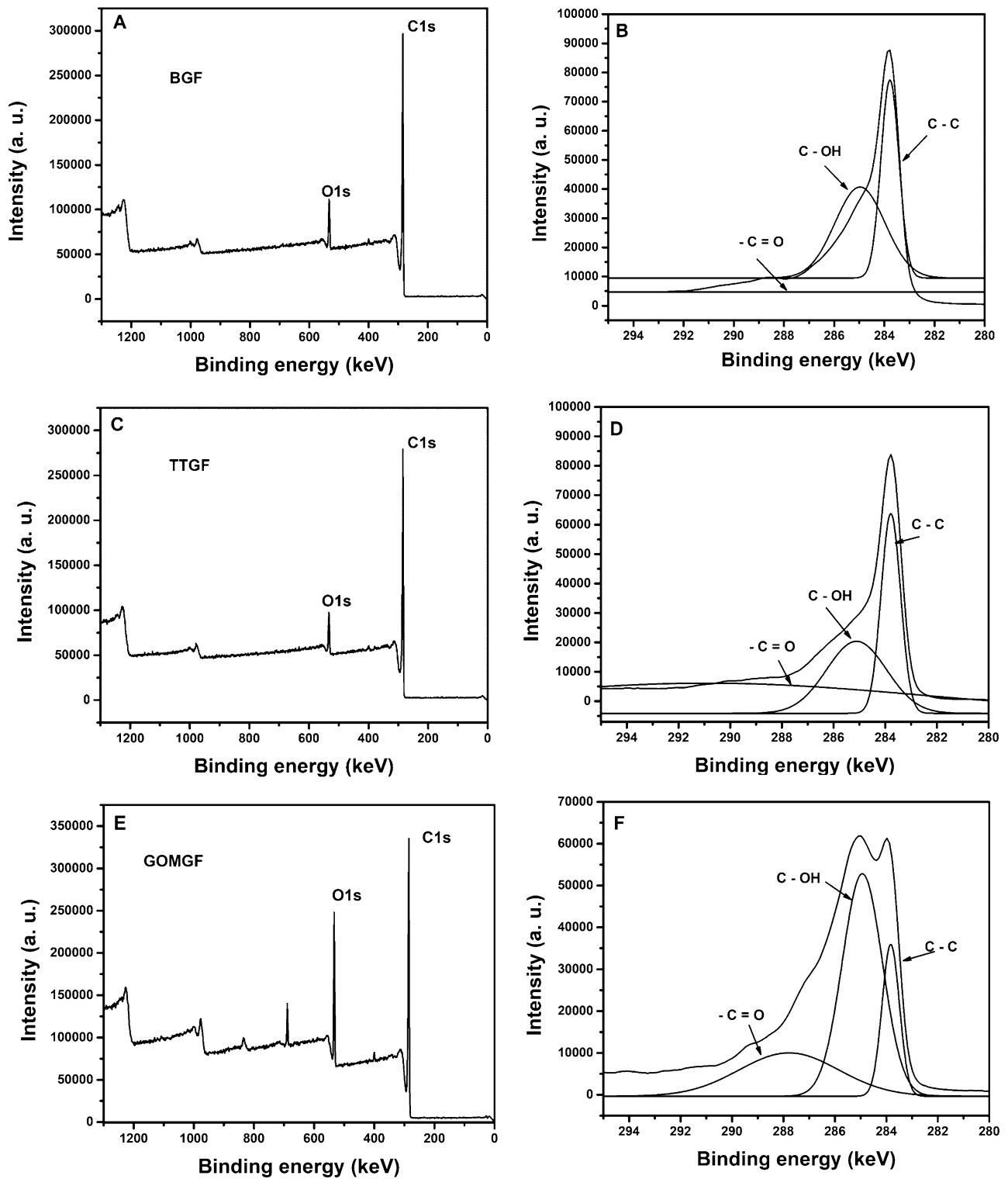
$$t = \frac{k\lambda}{\beta \cos \theta} \quad (7)$$

where  $k$  is a dimensionless shape element, which determines the particle's size ( $k=0.9$ ),  $t$  is the mean size of the ordered (crystalline) domain,  $\theta$  is the Bragg angle,  $\lambda$  is the X-ray

wavelength and  $\beta$  is the full width at half-maximum of the peak (in radians).

Morphology of GO, BGF, TTGF and GOMGF electrodes is shown in Fig. 3. GO had disordered layers of nanoflake agglomerates with wrinkle-like appearance as seen from Fig. 3a. In Fig. 3b and c, the microwire morphology of BGF and TTGF electrodes can be observed. The active surface of graphite wires is clearly evident in TTGF electrode than BGF electrode due to the effective thermal treatment. Figure 3d–h shows SEM images of the GOMGF electrodes with an increasing weight of the GO particles from 1 to 5 mgcm<sup>-2</sup>. The nano flaked layers of GO were finely and uniformly deposited on the surface of the GF electrodes. The deposited GO flakes are porous, wrinkled and have a unique structure with more active sites of oxygenated moieties, which are responsible for the enhancement of electrocatalytic activity in 4 mgcm<sup>-2</sup>-GOMGF electrode. Elemental analysis of the 4 mgcm<sup>-2</sup>-GOMGF electrodes indicated only carbon and oxygen elements as shown in Fig. 3i.

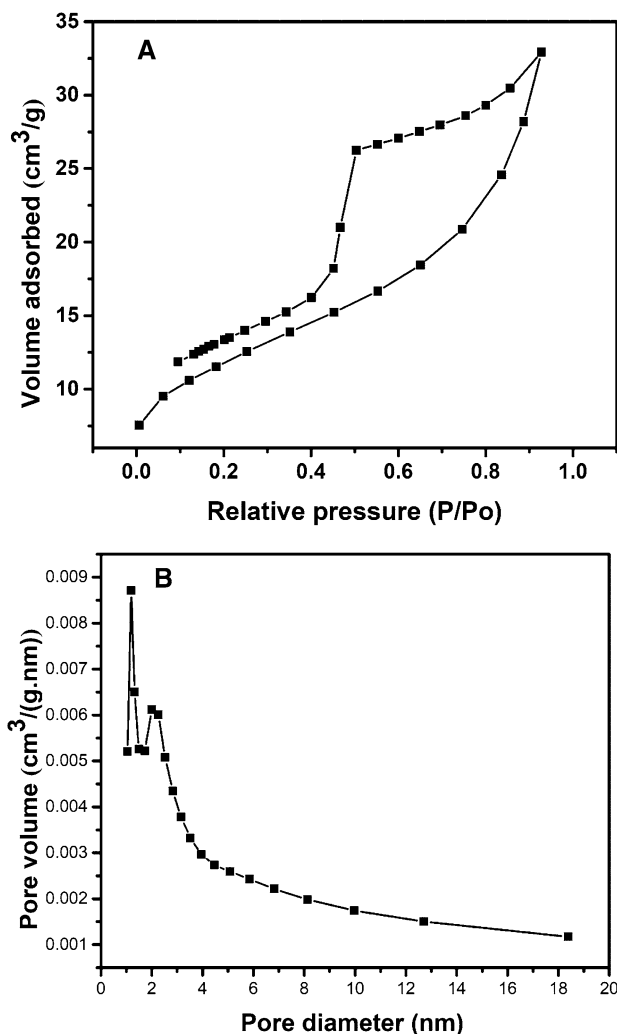
Figure 4 represents the Raman spectrum of the BGF, TTGF and 4 mgcm<sup>-2</sup>-GOMGF electrodes. The D and G band peaks for BGF and TTGF electrodes are represented at 1347.97 cm<sup>-1</sup>, 1358.08 cm<sup>-1</sup> and 1590.59 cm<sup>-1</sup>, 1600.69 cm<sup>-1</sup>, respectively. The G band of TTGF electrode was higher compared to BGF, probably due to the oxidation of GF during thermal treatment. The  $I_D/I_G$  value of the BGF and TTGF electrodes were 1.211 and 1.106. 4 mgcm<sup>-2</sup>-GOMGF electrodes showed strong D and G bands at 1347.97 cm<sup>-1</sup> and 1585.14 cm<sup>-1</sup>. The ratio of intensities ( $I_D/I_G$ ) was 1.008. 4 mgcm<sup>-2</sup>-GOMGF electrode showed less  $I_D/I_G$  value than the BGF and TTGF electrodes due to the modification of GO on the GF. The increase in defects and disorders in the 4 mgcm<sup>-2</sup>-GOMGF due to oxygen-containing functional groups on the graphitic planes of GO, leads to more active adsorption points or reactive



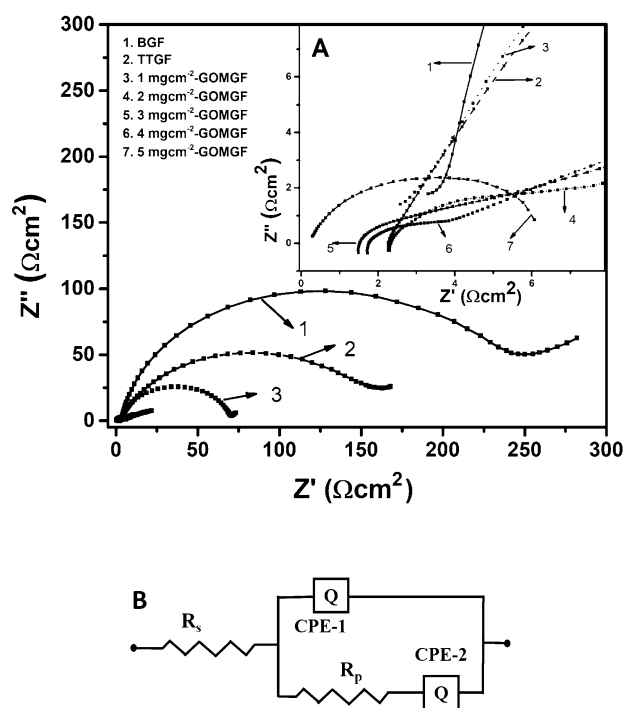
**Fig. 5** XPS spectra of survey and deconvoluted C1s spectra of BGF electrode (a and b), TTGF electrode (c and d) and GOMGF electrode (e and f)

**Table 1** Relative percentages of functional groups on the sample surfaces (%)

Samples	Elements		
	C1 <sub>s</sub>	O1 <sub>s</sub>	O/C ratio
BGF	96.36	3.64	0.037
TTGF	95.85	4.15	0.043
GOMGF	80.65	19.35	0.239

**Fig. 6** **a** Nitrogen adsorption–desorption isotherms and **b** corresponding pore size distribution curve of the GO

places for the electrode reactions causing high performance of electrochemical behavior toward the Fe<sup>2+</sup>/Fe<sup>3+</sup>

**Fig. 7** **a** EIS plots of BGF, TTGF and GOMGF electrodes. **b** Randles equivalent circuit of the BGF, TTGF and GOMGF electrodes**Table 2** Parameters obtained by fitting the Nyquist plots

Material	R <sub>s</sub> (Ω)	R <sub>p</sub> (Ω)
BGF	3.27	246.36
TTGF	2.64	159.36
1 mgcm <sup>-2</sup> -GOMGF	2.21	67.94
2 mgcm <sup>-2</sup> -GOMGF	2.26	5.81
3 mg cm <sup>-2</sup> -GOMGF	1.68	3.63
<b>4 mgcm<sup>-2</sup>-GOMGF</b>	<b>1.44</b>	<b>2.06</b>
5 mgcm <sup>-2</sup> -GOMGF	2.24	5.25

The important outcome of the present study are given in bold

reactions and vice versa [25, 26]. The same disorders were also observed in the SEM analysis.

Figure 5 presents the XPS spectra of BGF, TTGF and 4 mgcm<sup>-2</sup>-GOMGF electrodes and curves fitted with C1<sub>s</sub> deconvoluted spectra. The important peaks obtained upon deconvolution of C1<sub>s</sub> spectra were observed at 284.5 eV to C–C sp<sup>2</sup>, whereas for C–OH and –C=O at 286.3 eV and 288.3 eV, respectively. On analyzing the spectra of modified electrode samples, the peak intensities of the C–C functional groups decreased from BGF

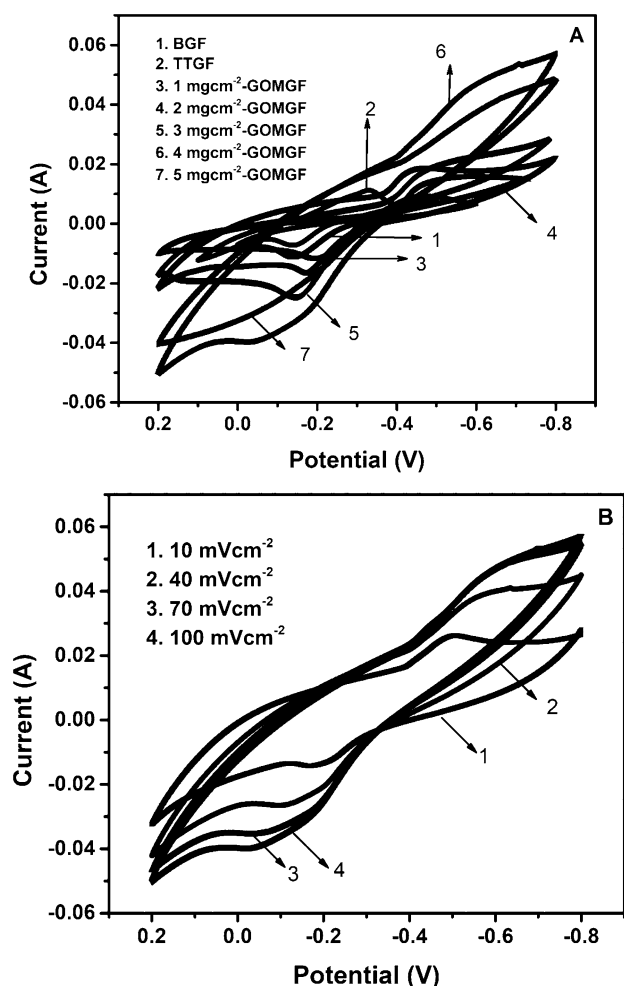


**Fig. 8** **a** Cyclic voltammograms of various electrodes at a scan rate of  $30 \text{ mVs}^{-1}$ . **b** Variation of scan rate using a  $4 \text{ mgcm}^{-2}$ -GOMGF electrode

to  $4 \text{ mgcm}^{-2}$ -GOMGF electrodes but an increase in peak intensities of the  $-\text{C}=\text{O}$  and  $\text{C}-\text{OH}$  functional groups indicates an increase in the percentage of oxygen of the  $4 \text{ mgcm}^{-2}$ -GOMGF electrodes. Table 1 substantiates the increase of oxygen level in the  $4 \text{ mgcm}^{-2}$ -GOMGF electrodes based on the relative oxygen percentage of 19.35 and the O/C ratio of 0.239. These values were higher

compared to the BGF and TTGF which may enhance reactive sites on the surface of the  $4 \text{ mgcm}^{-2}$ -GOMGF electrodes and improve the electrocatalytic activity [27].

Figure 6a shows the BET analysis of adsorption–desorption isotherms and Fig. 6b represents the pore distribution of GO in the  $\text{N}_2$  atmosphere. In adsorption–desorption isotherm the relative pressure was observed between 0.2 and 0.9 represents the Type IV isotherm. During desorption, broadening of curve were observed, indicates the H2(a) hysteresis loop with maximum microspores. Pore size distribution curve represents the intense peak less than 2 nm and small peak around the 3 nm shows the maximum of micro pore and minimum mesoporous in nature were confirmed from the BJH and  $t$ -plots. The average pore size was in the range of 1 to 4 nm. The surface area of the GO material was  $41.316 \text{ m}^2/\text{g}$ . These properties of GO improved the electrocatalytic activity of the  $4 \text{ mgcm}^{-2}$ -GOMGF electrode, shows better characteristic results in all electrochemical and performance studies.

### 3.1 Electrochemical analysis

EIS measurements were carried out for BGF, TTGF and GOMGF electrodes in  $\text{FeCl}_2$  electrolyte and the results are shown in Fig. 7a. The spectra obtained show a similar pattern of a depressed capacitive semi-circle in the high-frequency region, whereas a sloping straight line in the low-frequency region.  $R_s$  is bulk solution resistance and  $R_p$  is Faradaic interfacial charge-transfer resistance. It is important parameters indicating the capacity of the electrolyte and working electrodes.  $R_s$  and  $R_p$  of BGF, TTGF and GOMGF electrodes were compared with the Randles equivalent circuit is shown in Fig. 7b and values are listed in Table 2. The  $R_s$  of all the electrodes were around  $2 \Omega$ , except BGF which has a considerably higher  $R_s$   $3.27 \Omega$ . The  $4 \text{ mgcm}^{-2}$ -GOMGF electrode provides the least  $R_p$  value of  $2.06 \Omega$ , which may be due to the presence of  $-\text{OH}$ ,  $-\text{COOH}$  functional groups on the surface of the electrodes and other active sites which enhances the redox reaction of the  $\text{FeCl}_2$  electrolyte at the interface of the electrode. The resistance of the GOMGF was lowest up to a certain extent of modification, beyond which

**Table 3** Electrochemical parameters obtained from CV curves

Electrode	$I_{pa}$ ( $\text{mAcm}^{-2}$ )	$I_{pc}$ ( $\text{mAcm}^{-2}$ )	$I_{pa}/I_{pc}$	$E_c$ (V)	$E_a$ (V)	$\Delta E$ (V)
BGF	$8.769\text{e}^{-3}$	$5.389\text{e}^{-3}$	1.627	0.458	0.131	0.389
TTGF	$2.794\text{e}^{-3}$	$3.291\text{e}^{-3}$	0.848	0.032	0.295	0.263
$1 \text{ mgcm}^{-2}$ -GOMGF	$1.141\text{e}^{-3}$	$8.092\text{e}^{-3}$	0.141	0.199	0.496	0.297
$2 \text{ mgcm}^{-2}$ -GOMGF	$1.046\text{e}^{-3}$	$6.515\text{e}^{-3}$	0.160	0.154	0.489	0.335
$3 \text{ mgcm}^{-2}$ -GOMGF	$1.351\text{e}^{-3}$	$1.171\text{e}^{-3}$	1.153	0.145	0.590	0.445
<b><math>4 \text{ mgcm}^{-2}</math>-GOMGF</b>	<b><math>1.921\text{e}^{-3}</math></b>	<b><math>1.802\text{e}^{-3}</math></b>	<b>1.066</b>	<b>0.147</b>	<b>0.325</b>	<b>0.178</b>
$5 \text{ mgcm}^{-2}$ -GOMGF	$1.030\text{e}^{-3}$	$7.426\text{e}^{-3}$	0.138	0.085	0.663	0.578

The important outcome of the present study are given in bold

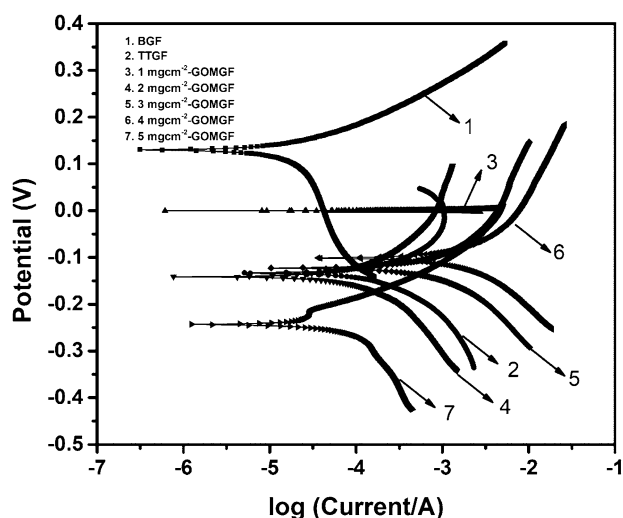


**Fig. 9** Tafel plot of BGF, TTGF and GOMGF electrodes

**Table 4** Linear polarization resistance value of the electrodes from the Tafel plot

Sample	Linear polarization resistance ( $\Omega$ )
BGF	1120
TTGF	322
1 mgcm <sup>-2</sup> -GOMGF	240
2 mgcm <sup>-2</sup> -GOMGF	191
3 mgcm <sup>-2</sup> -GOMGF	29
<b>4 mgcm<sup>-2</sup>-GOMGF</b>	<b>13</b>
5 mgcm <sup>-2</sup> -GOMGF	201

The important outcome of the present study are given in bold

the resistance increases due to the increase in the internal resistance of GO [28].

The CVs of BGF, TTGF and GOMGF electrodes are shown in Fig. 8a. 4 mgcm<sup>-2</sup>-GOMGF electrode showed a significant difference in the redox peaks compared to BGF, TTGF electrodes. Among all modified electrodes, 4 mgcm<sup>-2</sup>-GOMGF electrode exhibits the highest level of electrochemical performance. The relative CV which represents the difference of cathodic and anodic peak potential ( $\Delta E$ ) for 4 mgcm<sup>-2</sup>-GOMGF electrodes is around 0.178 V at a scan rate of 30 mVs<sup>-1</sup>. Similarly, the ratio of anodic ( $I_{pa}$ ) and cathodic ( $I_{pc}$ ) peak current densities is 1.066.  $\Delta E$  of the BGF and TTGF electrodes is 0.389 V and 0.263 V, respectively, the relative  $I_{pa}/I_{pc}$  values are 1.627 and 0.848 shows irreversible reactions toward the Fe<sup>2+</sup>/Fe<sup>3+</sup> redox reactions. The derived electrochemical data are given in Table 3. The lower  $\Delta E$  and ratio of  $I_{pa}$  and  $I_{pc}$  approaching 1 in 4 mgcm<sup>-2</sup>-GOMGF electrode indicates better reversibility and good electrochemical catalytic activity toward

Fe<sup>2+</sup>/Fe<sup>3+</sup> redox reactions. Figure 8b shows the CV variations as the scan rate changes from 10 to 100 mVs<sup>-1</sup>. The 4 mgcm<sup>-2</sup>-GOMGF electrode exhibits the best reversibility and electrochemical catalytic activity probably due to the appropriate modification of GO flakes. In addition to the better catalytic activity of GOMGF electrodes due to the presence of oxygenated disordered active sites, the wrinkled layers provide an effective surface for the oxidation of Fe<sup>2+</sup> to Fe<sup>3+</sup> and reduction of Fe<sup>2+</sup>/Fe<sup>0</sup> for the redox reaction of FeCl<sub>2</sub> system [29]. The CV studies have good agreement with the EIS analysis of GOMGF electrodes (weight cm<sup>-2</sup>) based on the  $\Delta E$  and  $I_{pa}/I_{pc}$  values.

Tafel plot of BGF, TTGF and GOMGF electrodes as shown in Fig. 9. From the Tafel plot of the electrodes calculated the linear polarization resistance values are given in Table 4. The calculated linear polarization resistance decreased from BGF, TTGF and 1 to 4 mgcm<sup>-2</sup>-GOMGF electrodes but 5 mgcm<sup>-2</sup>-GOMGF electrodes showed a sudden increase in the linear polarization resistance. Among all electrodes, 4 mgcm<sup>-2</sup>-GOMGF electrode provides a very low resistance of 13 ohms, whereas 5 mgcm<sup>-2</sup>-GOMGF electrode shows a much higher resistance of 201 ohms, which may be due to the increase in internal resistance because of high amount of GO on GF electrode [30]. SEM image also confirmed the high amount of GO on the surface of the 5 mgcm<sup>-2</sup>-GOMGF electrodes. The decrease in the linear polarization resistance value for modified electrodes may be due to the electrocatalytic activity of the heavily wrinkled nanoflake GO deposited on the GF electrode [31].

## 4 Performance characterization of single-cell flow battery

The charge–discharge studies were carried out using 132 cm<sup>2</sup> cell between current density of 10 to 40 mAcm<sup>-2</sup>. In the cell, BGF, TTGF and GOMGF electrodes were used as positive electrode and BGF as negative electrode. The efficiencies of the cell using BGF, TTGF and GOMGF electrodes were calculated and compared at 20 mAcm<sup>-2</sup>. The 4 mgcm<sup>-2</sup>-GOMGF electrode provides the best efficiencies than the BGF, TTGF and other GOMGF electrodes as shown in Fig. 10a. The corresponding  $\eta_C$  and  $\eta_E$  values are provided in Table 5. The 4 mgcm<sup>-2</sup>-GOMGF electrode shows good reversibility for the redox process of the FeCl<sub>2</sub> system (Fe<sup>2+</sup>/Fe<sup>3+</sup>), due to the lower charge-transfer resistance and lesser electrochemical polarization as observed in the electrochemical studies.

Figure 10b represents the performance of the 4 mgcm<sup>-2</sup>-GOMGF electrode at current densities between 10 and 40 mAcm<sup>-2</sup>. The  $\eta_C$   $\eta_E$  were between 50.05% to 65.94% and 41.08% to 42.02, respectively (Table 6).

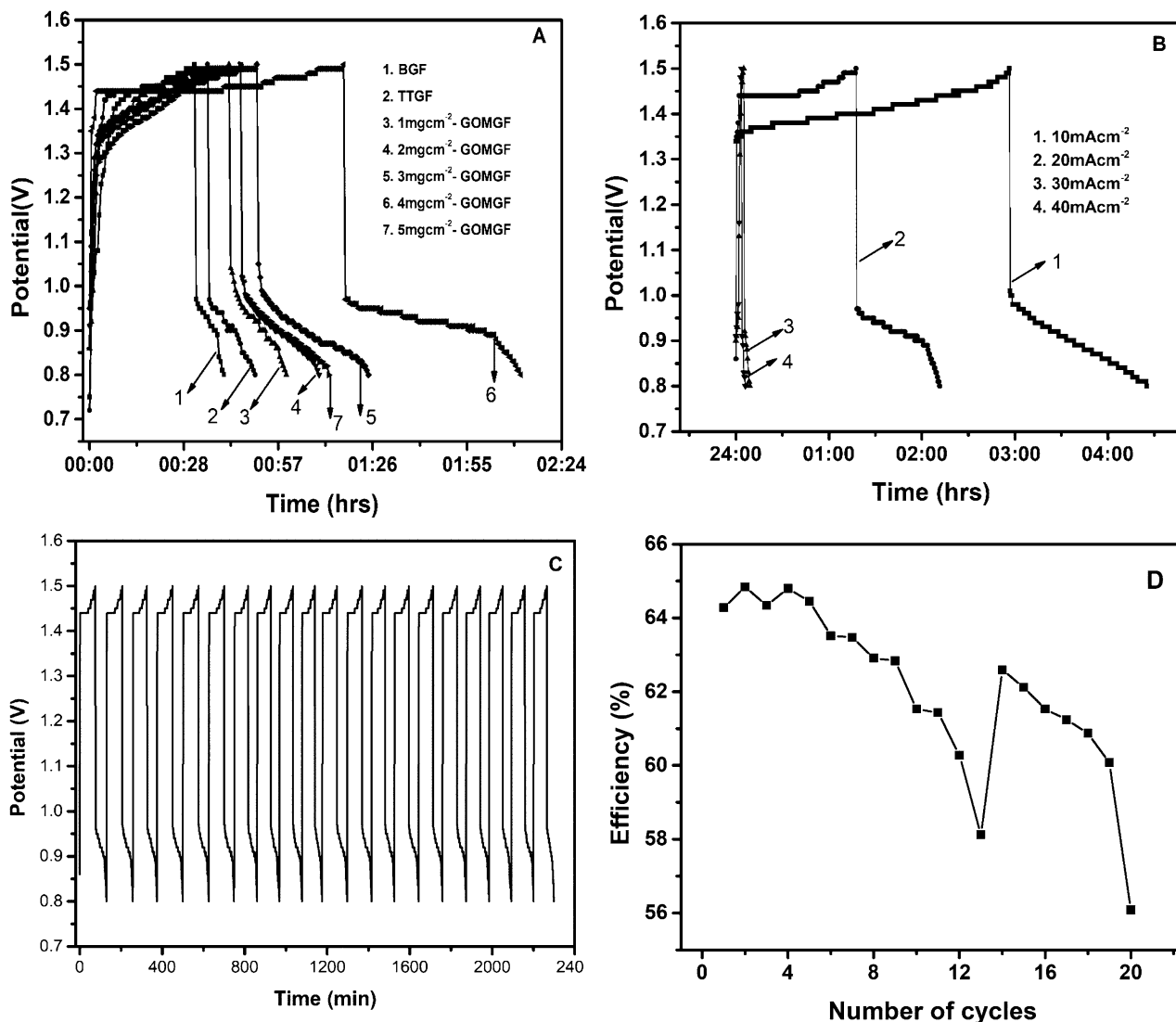


**Fig. 10** a Performance studies for BGF, TTGF and GOMGF electrodes. b Variation of current densities (10–40 mAcm<sup>-2</sup>) of 4 mgcm<sup>-2</sup>-GOMGF electrode. c Cyclic charge–discharge performance

of the 4 mgcm<sup>-2</sup>-GOMGF electrode at 20 mAcm<sup>-2</sup>. d Effect of  $\eta_C$  vs number of cycles

**Table 5** Battery performance characterization for all the electrodes at 20 mAcm<sup>-2</sup>

Electrode sample	Coulombic efficiency ( $\eta_C$ )	Voltaic efficiency ( $\eta_V$ )	Energy efficiency ( $\eta_E$ )
BGF	28.14	71.13	20.01
TTGF	38.33	73.24	28.07
1 mgcm <sup>-2</sup> -GOMGF	52.37	77.96	40.82
2 mgcm <sup>-2</sup> -GOMGF	54.73	75.51	41.32
3 mgcm <sup>-2</sup> -GOMGF	60.70	75.51	45.83
<b>4 mgcm<sup>-2</sup>-GOMGF</b>	<b>64.61</b>	<b>80.82</b>	<b>52.21</b>
5 mgcm <sup>-2</sup> -GOMGF	54.30	73.93	40.14

The important outcome of the present study are given in bold

**Table 6** Battery performance characterization using 4 mgcm<sup>-2</sup>-GOMGF electrode

Current densities (mAcm <sup>-2</sup> )	Coulombic efficiency ( $\eta_C$ )	Voltaic efficiency ( $\eta_V$ )	Energy efficiency ( $\eta_E$ )
10	50.05	82.08	41.08
20	64.61	77.81	50.27
30	65.29	71.67	46.79
40	65.94	63.73	42.02

**Table 7** Multiple cycling study of a cell using 4 mgcm<sup>-2</sup>-GOMGF electrode at 40 mAcm<sup>-2</sup>

Cycle number	Coulombic efficiency ( $\eta_C$ )	Voltaic efficiency ( $\eta_V$ )	Energy efficiency ( $\eta_E$ )
1	64.29	73.93	47.52
2	64.86	74.12	48.06
3	64.34	73.8	47.48
4	64.8	74.08	48.00
5	64.45	73.91	47.63
6	63.52	73.21	46.50
7	63.47	73.43	46.61
8	62.91	72.87	45.84
9	62.84	72.42	45.51
10	61.53	72.18	44.41
11	61.43	71.93	44.19
12	60.28	71.85	43.31
<b>13</b>	<b>58.12</b>	<b>68.74</b>	<b>39.95</b>
14	62.59	72.41	45.32
15	62.12	72.18	44.84
16	61.53	71.87	44.22
17	61.24	71.74	43.93
18	60.87	70.16	42.71
19	60.08	69.95	42.03
20	56.08	64.53	36.19

The important outcome of the present study are given in bold

In addition, the stability of the cell was studied using 4 mgcm<sup>-2</sup>-GOMGF electrode as shown in Fig. 10c and results obtained are included in Table 7. The evolution  $\eta_C$  of 4 mgcm<sup>-2</sup>-GOMGF electrode was plotted against the number of cycles as shown in Fig. 10d. The  $\eta_C$  for 1st cycle was found to be 64.29% which increases to 64.86% at 2nd cycle, but decreases gradually and becomes 56.08% at 13th cycle this decrease in  $\eta_C$  was attributed the inactivity of membrane. Membrane was cleaned using dilute HCl and charge–discharge studies were continued up to 20th cycle. The average  $\eta_C$  and  $\eta_E$  were found to be 62.06% and 42.02%, respectively, after 20th cycles. It has been found

that  $\eta_C$  start decreasing further after 20th cycle due to loss of stability of the electrolyte. At a current density of 40 mAcm<sup>-2</sup>  $\eta_C$  and  $\eta_E$  was 64.80% and 48.0%, respectively. The modification of GF with GO was enhanced the charge/discharge and cycle performance of the IRFB.

Most of the reports on all-iron flow batteries use non-aqueous iron electrolytes with three-electrode systems and active areas lesser than 25 cm<sup>2</sup> of cells. Few studies also reported aqueous iron electrolytes and their work mainly focused on the ligand optimizations [32–36]. The performance of iron flow batteries made using different sizes of cells is compared in Table 8. The cells used in the literature in IRFBs are produced performance efficiencies of 90–97% with lower current densities lesser or equal to 10 mAcm<sup>-2</sup>. The non-aqueous iron electrolytes used in the IRFBs systems were not economical and also pose a hazard to the environment, but aqueous electrolytes are eco-friendly. In this work, aqueous iron-electrolyte is used for performance characteristics of 132 cm<sup>2</sup> cells. The 4 mgcm<sup>-2</sup>-GOMGF electrode was produced 65.94% columbic efficiency as compared with the BGF electrode (28.14%).

## 5 Conclusions

GO synthesized using modified Hummer's method had a nanoflake structure. Synthesized GO was used to modify GF electrode by electrostatic spraying after ultrasonic treatment. Performance characterization of BGF, TTGF and GOMGF electrodes was studied using FeCl<sub>2</sub> as an electrolyte. At 20 mAcm<sup>-2</sup>, the 4 mgcm<sup>-2</sup>-GOMGF electrode exhibits good charge/discharge characteristics with a  $\eta_C$  and  $\eta_E$  of 64.61% and 50.27%, respectively. 4 mgcm<sup>-2</sup>-GOMGF electrode also had good agreement with all electrochemical studies and structural characterizations. Therefore, the modification of the GF electrode could be efficiently and effectively tuned to obtain the desired surface activity and properties of the electrode. Although the flow battery exhibits relatively average

**Table 8** Performance characterization of various cell in an iron electrolytes

Positive electrode	Electrolyte	Coulombic efficiency ( $\eta_C$ ) (%)	Area of electrode (cm <sup>2</sup> )	References
Iron rod	Iron (II) chloride, Iron (II) sulfate	97	1	[32]
Porous carbon paper	Iron(III) chloride, Iron(III) sulfate	90	10	[33]
Glassy carbon	Iron-triethanolamine, Iron-cyanide	93	–	[34]
Graphite rod	Iron-triethanolamine/bromide	82.4	0.103	[35]
Rotating disk glassy carbon	Iron (II) chloride,	97	25	[36]
Rayon graphite felt (4 mgcm <sup>-2</sup> -GOMGF)	<b>Iron (II) chloride</b>	<b>65.4</b>	<b>132</b>	<b>This study</b>

The important outcome of the present study are given in bold

efficiency, the cyclic performance analysis reveals that all-iron aqueous electrolytes are potentially feasible. The  $\eta_C$  and  $\eta_E$  can be further increased by modifying the electrolytes. Furthermore, optimizing the electrolyte, selecting appropriate membranes and optimizing the electrocatalyst may lead to better performance of IRFBs and needs to be explored.

**Acknowledgements** The authors gratefully thank the Department of Science and Technology (DST), India, for financial support under MES scheme 2016. We also thank the Centre for Incubation, Innovation, Research and Consultancy (CIIRC), Jyothy Institute of Technology and Sri Sringeri Sharadha Peetham for supporting this research.

## References

- Flox C, Skoumal M, Rubio-Garcia J, Andreu T, Morante JR (2013) Strategies for enhancing electrochemical activity of carbon-based electrodes for all-vanadium redox flow batteries. *Appl Energy* 109:344–351
- Jin JF, Liu X, Liu Q, Wei Y, Niu Z, Zhang K (2013) Identifying the active site in nitrogen-doped graphene for the  $VO^{2+}/VO^{2+}$  redox reaction. *ACS Nano* 7(6):476–4773
- Chen JJ, Symes MD, Cronin L (2018) Highly reduced and protonated aqueous solutions of  $[P_2W_{18}O_{62}]_6^-$  for on-demand hydrogen generation and energy storage. *Nat Chem* 10(10):1042–1047
- Lin K-B, Beh R, Tong ES, Chen L, Valle Q, Aspuru-Guzik A, Aziz A, Gordon MJ, Roy G (2016) A redox-flow battery with an alloxazine-based organic electrolyte. *Nature Energy* 1(9):16102
- Huskinson B, Marshak MP, Suh C, Er SG, Michael RG, Cooper JC (2014) A metal-free organic–inorganic aqueous flow battery. *Nature* 505(7482):195
- Janoschka T, Martin N, Martin U, Friebe C, Morgenstern S, Hiller H (2015) An aqueous, polymer-based redox-flow battery using non-corrosive, safe, and low-cost materials. *Nature* 527(7576):78
- Beh ES, De Porcellinis D, Gracia RL, Xia KT, Gordon RG, Aziz MJ (2017) A neutral pH aqueous organic–organometallic redox flow battery with extremely high capacity retention. *ACS Energy Lett* 2(3):639–644
- Orita A, Verde MG, Sakai M, Meng YS (2016) A biomimetic redox flow battery based on flavin mononucleotide. *Nat Commun* 7:13230
- Janoschka T, Martin N, Hager MD, Schubert US (2016) An aqueous redox-flow battery with high capacity and power: the TEMPTMA/MV system. *Angew Chem Int Ed* 55(46):14427–144230
- Sevov CS, Hickey DP, Cook ME, Robinson SG, Barnett S, Minteer SD, Sigman MS (2017) Physical organic approach to persistent, cyclable, low-potential electrolytes for flow battery applications. *J Am Chem Soc* 139(8):2924–2927
- Liu T, Wei X, Nie Z, Sprenkle V, Wang W (2016) A total organic aqueous redox flow battery employing a low cost and sustainable methyl viologen anolyte and 4-HO-TEMPO catholyte. *Adv Energy Mater* 6(3):1501449
- Jayathilake B, Plichta E, Hendrickson M, Narayanan S (2018) Improvements to the coulombic efficiency of the iron electrode for an all-iron redox-flow battery. *J Electrochem Soc* 165(9):1630–1638
- Ferreira E, Giacomelli C, Giacomelli F, Spinelli A (2004) Evaluation of the inhibitor effect of L-ascorbic acid on the corrosion of mild steel. *Mater Chem Phys* 83(1):129–134
- Jiang H, Zeng Y, Wu M, Shyy W, Zhao T (2019) A uniformly distributed bismuth nanoparticle-modified carbon cloth electrode for vanadium redox flow batteries. *Appl Energy* 240:226–235
- Wu X, Xu H, Lu L, Zhao H, Fu J, Shen Y, Xu P, Dong Y (2014)  $PbO_2$ -modified graphite felt as the positive electrode for an all-vanadium redox flow battery. *J Power Sour* 250:274–278
- Fetyan A, El-Nagar GA, Derr I, Kubella P, Dau H, Roth C (2018) A neodymium oxide nanoparticle-doped carbon felt as promising electrode for vanadium redox flow batteries. *Electrochim Acta* 268:59–65
- Maleki M, El-Nagar GA, Bernsmeier D, Schneider J, Roth C (2020) Fabrication of an efficient vanadium redox flow battery electrode using a free-standing carbon-loaded electrospun nanofibrous composite. *Sci Rep* 10(1):1–14
- Yang B, Hooper-Burkhardt L, Wang F, Surya Prakash GK, Narayanan SR (2014) An inexpensive aqueous flow battery for large-scale electrical energy storage based on water-soluble organic redox couples. *J Electrochem Soc* 161(9):1371–1380
- Cheng D, Tian M, Wang B, Zhang J, Chen J, Feng X, He Z, Dai L, Wang L (2020) One-step activation of high-graphitization N-doped porous biomass carbon as advanced catalyst for vanadium redox flow battery. *J Colloid Interface Sci* 572:216–226
- Li W, Liu J, Yan C (2013) Reduced graphene oxide with tunable C/O ratio and its activity towards vanadium redox pairs for an all vanadium redox flow battery. *Carbon* 55:313–320
- Gonzalez Z, Botas C, Blanco C, Santamaria R, Granda M, Alvarez P, Menendez R (2013) Graphite oxide-based graphene materials as positive electrodes in vanadium redox flow batteries. *J Power Sour* 241:349–354
- Bayeh AW, Kabtamu DM, Chang YC, Chen GC, Chen HY, Lin GY, Liu TR, Wondimu TH (2018) Synergistic effects of a  $TiNb_2O_7$ -reduced graphene oxide nanocomposite electrocatalyst for high-performance all-vanadium redox flow batteries. *J Mater Chem A* 6(28):13908–13917
- Chakrabarti B, Nir D, Yufit V, Tariq F, Rubio Garcia J, Maher R, Kucernak A, Aravind PV, Brandon N (2017) Performance enhancement of reduced graphene oxide-modified carbon electrodes for vanadium redox-flow systems. *ChemElectroChem* 4(1):194–200
- Zaaba N, Foo K, Hashim U, Tan S, Liu WW, Voon C (2017) Synthesis of graphene oxide using modified hummers method: solvent influence. *Procedia Eng* 184:469–477
- Han P, Wang H, Liu Z, Chen X, Ma W, Yao J, Zhu Y, Cui G (2011) Graphene oxide nanoplatelets as excellent electrochemical active materials for  $VO^{2+}/VO^{2+}$  and  $V^{2+}/V^{3+}$  redox couples for a vanadium redox flow battery. *Carbon* 49(2):693
- Han P, Yue Y, Liu Z, Xu W, Zhang L, Xu H, Dong S, Cui G (2011) Graphene oxide nanosheets/multi-walled carbon nanotubes hybrid as an excellent electrocatalytic material towards  $VO^{2+}/VO^{2+}$  redox couples for vanadium redox flow batteries. *Energy Environ Sci* 4(11):4710–4717
- Gonzalez Z, Botas C, Alvarez P, Roldan S, Blanco C, Santamaria R, Granda M, Menendez R (2012) Thermally reduced graphite oxide as positive electrode in vanadium redox flow batteries. *Carbon* 50(3):828–834
- Li W, Zhang Z, Tang Y, Bian H, Ng TW, Zhang W, Lee CS (2016) Graphene-nanowall-decorated carbon felt with excellent electrochemical activity toward  $VO^{2+}/VO^{2+}$  couple for all Vanadium redox flow battery. *Adv Sci* 3(4):1500276
- Shi L, Liu S, He Z, Shen J (2014) Nitrogen-doped graphene: effects of nitrogen species on the properties of the vanadium redox flow battery. *Electrochim Acta* 138:93–100
- He Z, Li M, Li Y, Li C, Yi Z, Zhu J, Dai L, Meng W, Zhou H, Wang L (2019)  $ZrO_2$  nanoparticle embedded carbon nanofibers

- by electrospinning technique as advanced negative electrode materials for vanadium redox flow battery. *Electrochim Acta* 309:166–176
31. Seri O, Siree B (2017) The differentiating polarization curve technique for the tafel parameter estimation. *Catalysts* 7(8):239
  32. Hawthorne KL, Petek TJ, Miller MA, Wainright JS, Savinell RF (2015) An investigation into factors affecting the iron plating reaction for an all-iron flow battery. *J Electrochem Soc* 162(1):A108–A113
  33. Tucker MC, Phillips A, Weber AZ (2015) All-iron redox flow battery tailored for off-grid portable applications. *Chemsuschem* 8(23):3996–4004
  34. Gong K, Xu F, Grunewald JB, Ma X, Zhao Y, Gu S, Yan Y (2016) All-soluble all-iron aqueous redox-flow battery. *ACS Energy Lett* 1(1):89–93
  35. Wen YH, Zhang HM, Qian P, Zhou HT, Zhao P, Yi BL, Yang YS (2006) A study of the Fe (III)/Fe (II)–triethanolamine complex redox couple for redox flow battery application. *Electrochim Acta* 51(18):3769–3775
  36. Manohar AK, Aswin K, Kim KM, Plichta E, Hendrickson M, Rawlings S, Narayanan SR (2016) A high efficiency iron-chloride redox flow battery for large-scale energy storage. *J Electrochem Soc* 163(1):A5118–A5125

**Publisher's Note** Springer Nature remains neutral with regard to jurisdictional claims in published maps and institutional affiliations.